J Therm Anal Calorim (2011) 104:635–643
DOI 10.1007/s10973-010-1039-7

Thermal behavior and evolution of the mineral phases of Brazilian red mud

J. M. Rivas Mercury · A. A. Cabral · A. E. M. Paiva · R. S. Angélica · R. F. Neves · T. Scheller

Received: 30 June 2010 / Accepted: 3 September 2010 / Published online: 22 September 2010

Abstract This article studied the thermal behavior and the evolution of the crystalline phases with temperature of the red mud (bauxite tailing) from an aluminum industry at Maranhão, North-Northwestern Brazil. The experiments were carried out by Field Emission Scanning Electron Microscopy (FE-SEM), Simultaneous Thermal Analysis (TG–DSC), Optical Dilatometry up to 1623 K, and X-ray diffraction (XRD) of previously heated samples between 523 and 1523 K. The crystalline phases and the amorphous contents were quantified on raw and heated samples (at 1523 K) according to the Rietveld Quantitative Analysis (RQA) method. The data obtained showed that the raw red mud is composed by a mixture of seven different phases (hematite, goethite, sodalite, anatase, gibbsite, calcite, and amorphous). Finally in the interval of 1023–1523 K the following crystalline phases: hematite, nepheline, sodalite, anatase, perovskite, and pseudobrookite have been observed.

Keywords Red mud · Bauxite tailing · Thermal behavior · Rietveld

Introduction

Bauxite deposits are known to occur in at least 50 countries, with estimated world reserves of approximately 25 billion tones. The production of this raw material in 2007 was 190 million tones. Six countries are responsible for 84.7% of the world's production: Australia 33.7% (64 million metric dry tons (Mt)); China 16.8% (32 Mt); Brazil 12.6% (24 Mt); Guinea 7.4% (14 Mt); Jamaica 7.4% (14 Mt); and India 6.8% (13 Mt) [1].

The main mineral in bauxite ores is gibbsite, which is extracted in the Bayer process [2] to produce alumina (Al_2O_3), the most important compound of aluminum used in the production of aluminum metal in the Hall–Heroult process [3, 4]. Alumina production worldwide from bauxites by the Bayer's process is about 81.6 Mt/year, with a market value of approximately $ 9 billion per year, with a typical sale price of about $ 200/ton [5]. This process generates red mud, which is a solid waste with high concentration of sodium, high pH (>11), high alkalinity, and heavy metals contents [6].

Far from our knowledge, information about the Brazilian red mud production in the literature is scarce. However, according to the U.S. Geological Survey, the alumina production in this country reached the mark of 7 Mt in 2008 [1]. Taking into account that for each ton of alumina almost produced, 1–1.5 tons of mud red is generated [7]; it is possible to infer that the Brazilian red mud production is almost 7–10.5 Mt/year. If one takes into account the increasing of new investments for the alumina production in Barcarena, Paragominas and Jurity (Brazil), the amount of this residue should be multiplied by four, and could be estimated in around 22 Mt/year of this material in the next years [8].

The mineral and chemical compositions of the red mud depend mainly from the quality of bauxite and operational process parameters. In general, they are largely composed of iron oxides, hematite (Fe_2O_3), and goethite (FeOOH), aluminum oxide as the hydroxides gibbsite ($Al(OH)_3$), and

J. M. Rivas Mercury (✉) · A. A. Cabral · A. E. M. Paiva
Federal Institute of Education Science and Technology of Maranhão—IFMA, Sao Luis, Brazil
e-mail: rivascefetma@gmail.com

R. S. Angélica · R. F. Neves · T. Scheller
Geoscience Institute—IGC, Federal University of Para (UFPA), Belem, Brazil

boehmite (AlOOH), calcium oxides, titanium oxides (anatase and rutile), and aluminosilicate minerals (sodalite) [7, 9–11].

In addition, the Brazilian Standards Association (ABNT) classifies the red mud as a dangerous waste due to their high alkalinity and heavy metals content (high corrosive and high reactivity). Therefore, its inadequate manipulation can cause serious environmental and economical problems [12].

Many attempts of taking advantage of this residue have been carried out [13–21]. Several researchers have also studied red mud from different sources by thermal analysis and other techniques [22–27]. All of them have reported that this material has a complex behavior due to their chemical and mineralogical composition. Therefore, the knowledge of this material is necessary to plan any production process. In spite of the importance of the Brazilian aluminum industry, there are no registries about the thermal behavior of the Brazilian Red Mud (BRM) in the literature.

The aim of this article was to study the thermal behavior and the phase transformations during the heating of a Brazilian Red Mud, hereinafter called as BRM, using the following techniques: Wet chemical Analysis and Atomic Absorption Spectrometry (AAS), X-ray powder diffraction (XRD), Rietveld Quantitative Analysis (RQA), thermal analysis (Thermogravimetry, Differential Scanning Calorimetry, and Optical Dilatometry). The morphology of the powder samples were also investigated by Scanning Electron Microscopy.

Experimental

Sample preparation

A plastic drum (250 kg) of red mud from the aluminum industry of São Luis-Maranhão (Alcoa) with pH 12.9 was received in laboratory, being that approximately 5 kg was separated and dried at room temperature (305 K) and at 333 K in a forced air oven. Almost 250 g of this material, hereinafter called as Brazilian Red Mud (BRM), was disaggregated and sieved through the 100 mesh, which was used for all experiments.

Physical characterization of the BRM powder

Specific surface area

The specific surface area (Se) of the BRM powder was analyzed by nitrogen gas adsorption on the solid surface according to B.E.T. (Brunauer, Emmet e Teller) Theory, in a Monosorb Surface Area Analyzer; model MS-13, of Quantachrome Corporation.

Particle size distribution

The particle size distribution was carried out using a laser scattering-based size analyzer (Master Sizer S; Malvern Instruments, UK). The measurements were realized on slurry sample. Sodium hexametaphosphate was used as dispersant, and the particles were further desaglomerated by an ultrasonic treatment of 5 min.

True density

The true density of the BRM powder was measured by He pycnometry, using a Micromeritics AccuPyc 1330 instrument.

Chemical analysis

The chemical analysis was done by several methods as follows: SiO_2 and Loss of Ignition (LOI) by gravimetry; Al_2O_3—complexometry; and Fe_2O_3 total and TiO_2 by colorimetry. The alkaline elements (CaO, MgO, Na_2O, and K_2O) were determined by absorption, in a Perkin Elmer 3300 Atomic Absorption Spectrometer.

Thermal analysis

Heating experiments under static atmosphere

Static heating in air of ca. 3 g of BRM was carried out in a furnace at the temperature range 523–1523 K (normal pressure conditions) with a constant heating rate of 10 K/min and 1 h of dwell time. The powders obtained were ground in an Agatha mortar and analyzed by XRD to identify the mineral changing of the specimens with temperature.

Conventional thermal analysis

Differential Scanning Calorimetry (DSC) and Thermogravimetric (TG) analysis were conducted at a constant heating rate of 5 K/min up to 1623 K in blowing air (50 cm^3 min^{-1}), using Pt crucibles and α-Al_2O_3 powder as the reference in an STA 449 C equipment from Netzsch. All acquired data were normalized for 10 mg, with baseline correction.

Optical dilatometry

Cylindrical pressed pellets of 50 mm of diameter were conformed at 5 MPa and heated up until 1623 K with a constant heating rate of 10 K/min. The dimensional changing of the BRM with the heating were analyzed by an

Optical Dilatometer (EM201—Hesse Instrument, Osterode am Harz—Germany).

X-ray diffraction analysis

X-ray diffraction (XRD) analysis was carried out using monochromatic CuKα (0.15406 nm) anode in an X'Pert PRO (MPD PW 3040/60 Theta/Theta of PANalytical (B.V.) Diffractometer with an RTMS X'Celerator detector. The crystalline phases in the BRM samples were identified and compared with the powder diffraction files cards (PDF): PDF 033-0664 (Hematite), PDF 081-0464 (Goethite), PDF 070-2038 (Gibbsite), PDF 085-2065 (Sodalite), PDF 071-1167 (Anatase), PDF 086-0174 (Calcite), PDF 083-2279 (Nepheline), PDF 089-6949 (Perovskite), PDF 073-1631 (Pseudobrookite), and PDF 086-0174 (Quartz), using the software X'Pert HighScore version 2.1b (PANalytical) compiled by the International Center for Diffraction Data (ICDD).

Conventional XRD measurements

Conventional XRD patterns of the BRM and heated samples (523–1523 K) were acquired under the following conditions: voltage: 40 kV; current: 30 mA; scan range from 5 to 70° (2θ); step size of 0.017 (2θ); continuous scan mode; and time per step 5 s.

Quantitative XRD analysis

The quantitative mineralogical analysis by the Rietveld Method was carried out for two different groups of sample: (i) raw dry and unheated powders samples (BRMR), which were mixed with 20% in mass of CaF_2 (Merck, A.A.) as standard; (ii) heat-treated powders (1523 K) (BRMH), which were mixed with 10% in mass of Silicon metal (NIST) as pattern. Both samples were separately homogenized in a mixer mill during 5 min, in an Agatha jar, with Agatha balls, and the XRD patterns were acquired under the following conditions: 40 kV; 35 mA; scan range from 10 to 90° (2θ); step size of 0.017 (2θ); continuous scan mode; time per step 81 s. In order to quantify the mineral phases in both samples of BRM, Rietveld Quantitative Analysis (RQA) was carried out using Fullprof Suite package programs [28].

Scanning electron microscopy

The morphology of the BRM powder was investigated by field emission scanning electron microscopy (FE-SEM), Hitachi S-4700 (Hitachi, Tokyo, Japan). The powder surface was carefully coated with a thin Au–Pd layer by sputtering.

Results and discussion

Physical properties of BRM

Table 1 shows the physical properties (true density, specific surface area, and particle size/agglomerate) of the BRM (unheated powder). The obtained average particle/agglomerate size, D_{50}, was almost 3.80 μm. Otherwise, the maximum size, D_{90}, was 8.42 μm with a Specific surface area (Se) of 12.96 $m^2\ g^{-1}$, and a true density of 2.65 g cm^{-3}.

These results indicate that the BRM is similar to other investigated red mud [9, 10, 14], has small particle/agglomerate sizes, and a high specific surface area. This very important feature should be taken into account for the application of these wastes as raw material.

From the FE-SEM micrography showed in Fig. 1a, one can observe that BRM powder is constituted by agglomerates less than 10 μm, formed by very fine particles of different sizes. In Fig. 1b, one can also observe the presence of agglomerated porous with flakes morphology, which are smaller than 3 μm.

Chemical analysis and mineralogy

Table 2 shows the chemical composition of the BRM and of other red mud reported in the literature [11, 16, 19, 26, 27]. It is possible to observe that BRM, like others red mud, is constituted by a mixture of Fe_2O_3, Al_2O_3, SiO_2, Na_2O, TiO_2, MgO, and CaO, which are the majority oxides. The K_2O is also present, but in less quantities.

Mineral identification and quantitative analysis

The conventional XRD analysis of the BRM powder was possible to identify the following mineral phases: hematite, goethite, gibbsite, quartz, sodalite, anatase, and calcite. In addition, an amorphous phase can be inferred by the high background observed that could be also due to the iron fluorescence. Phases with MgO content were not detected.

The RQA results and the difference curve of the BRM material are presented in Table 3 and Fig. 2. As one can see, the values calculated by RQA are in good agreement with the chemical analysis (Table 2), and the major

Table 1 Physical properties of the BRM powder

Properties	
ρ (g cm^{-3})	2.65
Se (B.E.T.) ($m^2\ g^{-1}$)	12.96
D_{10} (mm)	0.40
D_{50} (mm)	3.80
D_{90} (mm)	8.42

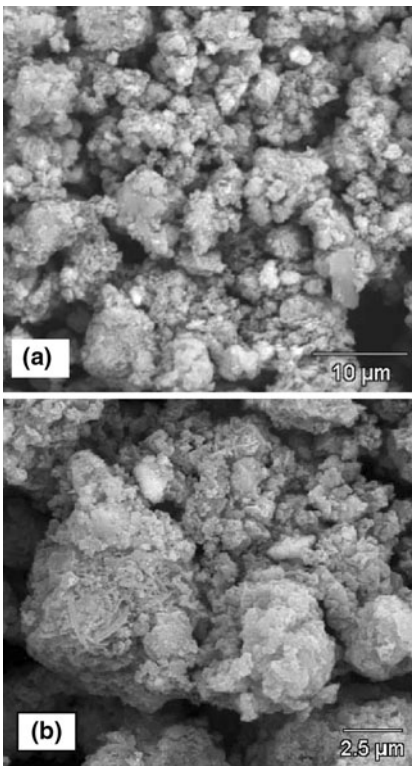

Fig. 1 SEM pictures of the BRM sample

Table 2 Chemical composition of BRM and data reported from others red mud reported in the literature

Mass/%				
Oxides	BRM*	Australia/10	Guine/9	Jamaica/14
Fe_2O_3	31.22	34.05	48.48	51.50
Al_2O_3	20.77	25.45	26.60	15.00
SiO_2	14.37	17.06	5.50	1.70
Na_2O	9.87	2.74	nr.	6.97
TiO_2	4.55	4.90	2.80	6.70
K_2O	0.20	nr.	nr.	nr.
CaO	2.49	3.69	1.20	7.0
MgO	3.92	1,86	0.90	nr.
LOI	12.61	10.25	14.52	11.13

nr. not reported, * This work

crystalline phases (64.3%) detected were: hematite, goethite, gibbsite, and sodalite. A high amorphous content of 24.9% was also observed. It is important to observe that this high amorphous content may be constituted by amorphous iron oxide, aluminum oxide, and silicon oxide, where the latter two are sometimes attributed to the desilication product (DSP) in the Bayer industry [29]. Another important feature of the RQA is that the technique is sensitive to the presence of phases comprising 1–2% of the

Table 3 Mineralogical composition of BRM and data reported from others red mud reported in the literature

Mineral phases	BRM* (mass/%)	Jamaica/14	Sapin/16	Turkey/39
Hematite	21.1	+++	+++	+++
Goethite	8.5	−	+	−
Sodalite	23.0	−	−	+++
Gibbsite	12.2	++	++	−
Anatase	4.1	+	+++	+
Calcite	2.3	+	+	+
Bohemite	nd.	+	+	+
Amorphous	24.8	+	+++	nr.
Quartz	4.1	+	−	+

* This work, $R_{wp} = 17.0$, $\chi^2 = 1.9$, Gof = 1.1

+++ Majoritary, ++ abundant, + detected, − absent

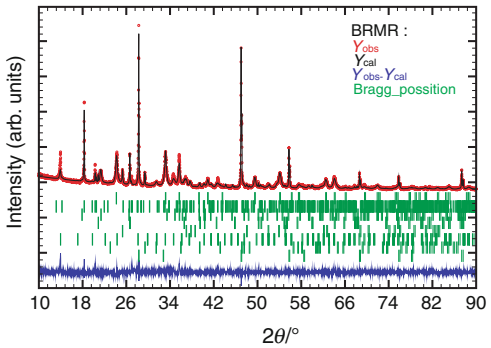

Fig. 2 Rietveld quantitative analysis of BRM and its difference curve

total, and the estimated standard error may be as large as 3–4% for the more abundant phases. This sensitivity is not to be ascribed to the numerical RQA method but mainly to the diffraction-pattern collection strategy. Aside from crystalline phases, experience with the background behavior of XRD patterns suggests that 10–25% of the BRM consisted of amorphous oxides. Taking into account the data set presented in Tables 2 and 3, one can asses that iron oxide is present in the sample as hematite and goethite; aluminum oxide as gibbsite and sodalite; titanium oxide as anatase; sodium oxide as sodalite; silicon oxide as quartz and sodalite; and calcium oxide as calcite. The BRM identified phases agree with those phases reported in the literature by other authors for red mud originated in different countries [30].

Red mud thermal behavior

TG and DSC measurements

The thermal behavior of the BRM obtained by TG/DSC is shown in Fig. 3. From the TG curve, one can observe that

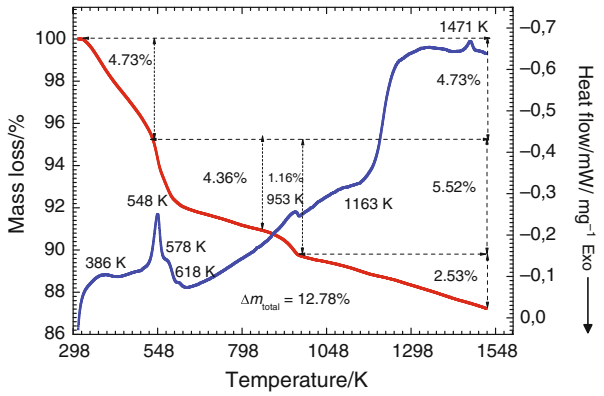

Fig. 3 Thermogravimetric and differential scanning calorimetry of the BRM

BRM presents a total mass loss of 12.78% until reaching 1523 K. The first mass loss (4.73%) occurs between 323 and 523 K, and it may be related to the free water evaporation and gibbsite decomposition. A second mass loss can be observed in the temperature range 533–964 K, and it can be attributed to goethite and calcite decomposition (overlap effects). The last one occurs between 965 and 1523 K, and it could be associated to the amorphous decomposition and to the sodalite contents, as it had been confirmed by RQA.

These thermal effects are better identified on the DSC curve, which confirms the previous results observed on the TG curve. Five endothermic effects are observed:

(i) a band centered at 386 K, which is associated to the physical water evaporation adsorbed on the particle surfaces;

(ii) at 548 K, an endothermic peak which is attributed to the thermal decomposition of gibbsite and a formation of a cryptocrystalline or a transition alumina (χ-Al_2O_3) [31, 32]. In this sense, the following reaction path is suggested [33, 34]:

$$\text{Gibbsite} \rightarrow \chi\text{-}Al_2O_3 \rightarrow \kappa\text{-}Al_2O_3 \rightarrow \alpha\text{-}Al_2O_3 \quad (1)$$

(iii) two weak endothermic peaks located at 578 and 618 K, which are associated to the goethite decomposition into hematite [35–37];

(iv) at 953 K, an endothermic peak that is related to the calcite decomposition [38, 39];

(v) at 1471 K; an endothermic peak which can be attributed to the sodalite decomposition [25, 39] or to the melting of the amorphous aluminosilicate materials found in the red mud [39].

Changes in the slope of the DSC curve also can be observed at 1163 K with no change associated in the TG curve. This change in the DSC curve could be associated to second-order transformations and the beginning of the sintering process of the sample.

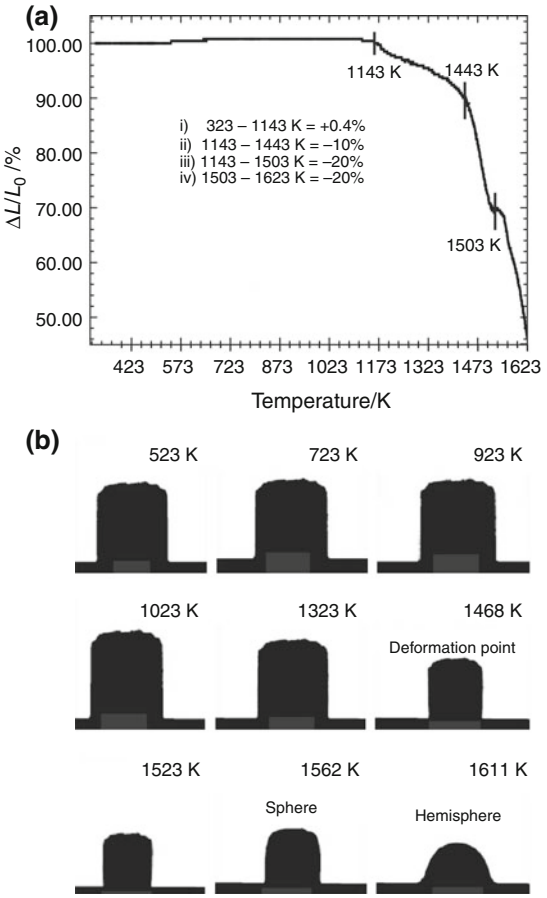

Fig. 4 Optical dilatometry of BRM: (**a**) dilatometric curve. **b** Photomicrographs of BRM during the heating experiments

Dilatometric measurements

The results of the optical dilatometry are presented in Fig. 4a and b, which reveal a very important feature of the thermal behavior of BRM as a function of the temperature. The material has a soft expansion of 0.4% until 1143 K that can be attributed to water, hydroxyl, or to CO_2 groups released during the decomposition of goethite, gibbsite, calcite, or α- to β-quartz transformation, as it has been observed by the XRD and TG–DSC experiments. Among 1143–1623 K, the sample shrinks approximately 50% according to the following steps: (i) 10% in the temperature range 1143–1443 K, which corresponds to the beginning of the sintering process; (ii) 20% among 1443–1503 K (the softening point); (iii) 20% above 1503 K, with the melting of the sample at 1623 K. From the sequences of pictures showed in Fig. 4b, it is also possible to observe that the sample almost does not suffer any dimensional changing

until 1123 K. However, as the temperature increases, it is easily observed that the sample shrinks (1323 K) and deforms at 1463 K. It should be emphasized that this temperature is close to the endothermic peak observed at 1471 K on the DSC curve. This hypothesis is confirmed if one takes into account that an increase of 333 K leads to an increase of 20% on the shrinkage, which indicates a strong liquid phase formation, being that the complete melting of the sample occurs at 1623 K.

Mineralogical phase evolution during heating

Figure 5 and Table 4 demonstrate the XRD analysis of the BRM crystalline phases as a function of the temperature. As one can observe in Table 4, the crystalline phases identified at 523 K were hematite, goethite, sodalite, gibbsite, quartz, anatase, calcite, and an amorphous. From 623 to 823 K, gibbsite and goethite were not detected, as it was observed by TG–DSC. Calcite and quartz disappear in the temperature range 923–1123 K (Fig. 5). Among 1223 and 1423 K the major crystalline phases identified were hematite, sodalite, nepheline, and pseudobrookite (Fe_2TiO_3). A small content of perovskite ($CaTiO_3$) was also detected. Finally, sodalite disappears at 1523 K and the only phases observed were hematite, nepheline, pseudobrookite, and perovskite. An increase of the amorphous band was also detected at small angles. The RQA carried out on the heat-treated sample at 1250 °C reveals that the final mineralogical composition of the BRM is: 43.4 ± 0.9% of hematite, 38.8 ± 0.6% of nepheline, 2.9 ± 0.4% of perovskite, 3. 9 ± 0.4% pseudobrookite, and 11.0 ± 0.4% of amorphous ($R_{wp} = 5.2$; $R_{exp} = 3.5$; $\chi^2 = 2.2$).

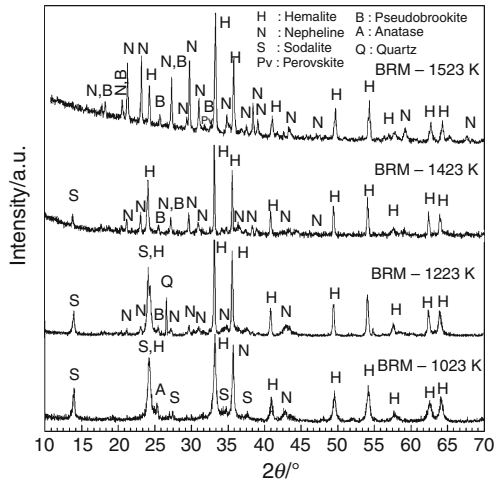

Fig. 5 Mineral phases identified after the heating of the BRM powder

Table 4 Mineral phases identified in the BRM after heating

Mineral phase	Temperature/K						
	523	623	723	823	923	1123	1323
Hematite	++	++	++	++	++	++	++
Sodalite	++	++	++	++	++	+	+
Gibbsite	+	−	−	−	−	−	−
Goethite	++	−	−	−	−	−	−
Quartz	++	++	+	+	+	−	−
Anatase	+	+	+	+	+	+	−
Calcite	+	+	+	+	−	−	−
Nepheline	−	−	−	−	−	+	++
Pseudobrookite	−	−	−	−	−	−	+
Perovskite	−	−	−	−	−	−	
Amorphous	++	++	++	++	++	+	+

++ Abundant, + detected, − absent

Reaction mechanism

Taking into account the TG–DSC curves (Fig. 3), optical dilatometry (Fig. 4), and the crystalline phase evolution (Fig. 5) during the heating identified by XRD and RQA, the following reaction mechanisms are proposed in this article:

(i) around 373–393 K water was adsorbed to the BRM particles, leaving the sample, as described below:

$$H_2O_{(l)} \rightarrow H_2O_{(g)} \quad (2)$$

(ii) among 523 and 553 K, gibbsite loses hydroxyl groups to form a cryptocrystalline alumina (Al_2O_3-k), as it follows:

$$2 \cdot Al(OH)_{3(s)} \rightarrow Al_2O_3\text{-}k_{(s)} + 3H_2O_{(g)} \quad (3)$$

Although this phase had been not detected by XRD, this statement is confirmed by other evidences, like the endothermic peak observed in the DSC curve at 543 K and the absence of reactions between 723 and 823 K (boehmite decomposition) in the TG–DSC curve [40–43].

(iii) Goethite dehydration takes place between 573 and 623 K, according to the following reaction [24, 35, 36, 44]:

$$2 \cdot FeO(OH)_{(s)} \rightarrow Fe_2O_{3(s)} + H_2O_{(g)} \quad (4)$$

From 661 to 1123 K, several reactions take place in the sample, as confirmed by the continuous mass loss observed in the TG curve. This fact is interpreted as the following:

(i) decomposition of calcite (1.16%) among 933–1023 K [38], as it can be observed in TG–DSC curve. This reaction occurs as described below:

$$CaCO_{3(s)} \rightarrow CaO_{(s)} + CO_{2(s)} \quad (5)$$

According to the literature, kaolinitic clay is present in most bauxites currently used for the production of alumina by the conventional Bayer process [5–7, 9]. During the refining process, this clay is attacked and dissolved into the Bayer liquor. The dissolved silica reprecipitates as a sodium aluminum silicate, also known as Bayer desilication product (DSP) or as Bayer-sodalite with the composition $3(Na_2O{\cdot}Al_2O_3{\cdot}2SiO_2)2NaX{\cdot}nH_2O$, where X represents a variety of inorganic anions, like sulfate, carbonate, chloride, aluminate, and hydroxide. This compound could be represented by [45]:

$$Na_{6+y}, [AlSiO_4]_6, (X)_y{\cdot}zH_2O; (0 \leq y \leq 2)]; \quad [(0 \leq z \leq 8) \quad (6)$$

(ii) as the temperature raises among 1023–1223 K, the BRM loses structural water yielding to the formation of nepheline or pseudonepheline as proposed by Borchert and Keidel for the heated NaOH and kaolinite [46]:

$$Na_{6+y}, [AlSiO_4]_6, (X)_y{\cdot}zH_2O \rightarrow Na_{6+y}, [AlSiO_4]_6, (X)_y{\cdot}nH_2O + (z-n)H_2O \uparrow \quad (7)$$

$$Na_{6+y}, [AlSiO_4]_6, (X)_y{\cdot}nH_2O \rightarrow (Na_2O)_{1/3}\, Na[AlSiO_4]_6 + (n + 1/2y)H_2O \uparrow \quad (8)$$

It is important to observe that sodalite is a feldespathoid mineral phase, which open structure can be stabilized by the different accommodated ions, leading to the increasing of the temperature of decomposition [47–49]. As one can observe in Fig. 5, sodalite disappears above 1423 K, indicating its complete decomposition. Among 1223 and 1523 K (Fig. 5), nepheline forms $[Na_{(1-2x)}{\cdot}M_xAlSiO_4; M = Li, K, Na, Ca - (0 < x \leq 0.5)]$, which can be explained by the reaction between amorphous aluminosilicates (DSP) and the sodalite decompositions products. For instance, the presence of gallium and alkaline earth or transition metals, which could be present in the lateritic soils like bauxite, turns out the statement about the Bayer process tailings inaccuracy, where the nepheline solid solution takes place after the heat treatment of BRM. The real final stoichiometry is described as below:

$$CaO_{(s)} + TiO_{2(s)} \rightarrow CaTiO_{3(s)} \quad (9)$$

$$Fe_2O_{3(s)} + TiO_{2(s)} \rightarrow Fe_2TiO_{5(s)} \quad (10)$$

The sequence of reactions above, representing the formation of perovskite and pseudobrookite in the temperature range 1123–1423 K, as detected by the X-ray diffraction experiments.

Conclusions

The mineral constitution of the Brazilian Red Mud was determined by X-ray diffraction and Rietveld Quantitative Analysis. The major crystalline phases (64.3%) detected were: hematite, goethite, gibbsite, and sodalite. A high amorphous content of 24.9% was also observed, which may be constituted by amorphous iron oxide, aluminum oxide, and silicon oxide. Several thermal events were observed by simultaneous TGA–DSC in the range from room temperature to 1673 K and were related to the composition of the sample. Decomposition reactions of gibbsite, goethite, calcite, and sodalite were observed on the DSC curve. The optical dilatometry experiments demonstrated that the BRM compacts do not suffer any dimensional changing until 1123 K. However, as the temperature increases, it is easily observed that the sample shrinks (1323 K) and deforms at 1463 K. The changing of the BRM mineral phases was followed as a function of the temperature by X-ray diffraction. At temperatures lower than 1123 K, the following crystalline phases were identified: hematite, goethite, sodalite, gibbsite, quartz, anatase, calcite, and an amorphous. Among 1123 and 1423 K the major crystalline phases identified were hematite, sodalite, nepheline, perovskite, and pseudobrookite (Fe_2TiO_3). At 1523 K, the final mineralogical composition of the BRM was also determined by Rietveld Quantitative Analysis as: 43.4 ± 0.9% of hematite, 38.8 ± 0.6% of nepheline, 2.9 ± 0.4% of perovskite, 3.9 ± 0.4% of pseudobrookite, and 11.0 ± 0.4% of amorphous.

Acknowledgements The authors wish to thank the Fundação ao Coordenação de Aperfeiçoamento de Pessoal de Nível Superior (CAPES) and Prof. Dr. José Anchieta Rodrigues at the Materials Engineering Department of The Federal University of São Carlos—São Paulo Brazil.

References

1. Bray EL. Bauxite and alumina. In: Survey USG, editor. Mineral commodity summaries 2008. Washington: US Geological Survey; 2008. p. 32.
2. Bayer KJ. 1972. German Patent No: 2150677.

3. Hall CM. 1889. US Patent No: 400766.
4. Heroult R. 1886. French Patent No: 175 711.
5. Authier-Martin M, Forté G, Ostap S, See J. The mineralogy of bauxite for producing smelter-grade alumina. JOM. 2001;53: 36–40.
6. Hinda AR, Bhargava SK, Grocott SC. The surface chemistry of Bayer process solids: a review. Colloids Surf A Physicochem Eng Asp. 1999. doi:10.1016/S0927-7757(98)00798-5.
7. Thakur RS, Saint BR. Utilization of red mud-part I. J Sci Ind Res. 1974;33:403–512.
8. Departamento Nacional de Produção Mineral: Brazilian Mineral data base. 2010. www.dnpm.gov.br. Accessed 30 Mar 2010.
9. Motta Sobrinho MA, Alves MCM, Silva Filho EB. Lama vermelha da indústria de beneficiamento de alumina: produção, características, disposição e aplicações alternativas. Revista Matér. 2007;12:322–38.
10. Glenister D, Smirk D, Piskersgil G. Bauxite residue-development of a resource. In: Proceedings of the international bauxite tailings workshop, Perth, Western Australia; 1992. p. 301–8.
11. Paranguru RK, Rath PC, Misra VN. Trends in red mud utilization—a review. Min Process Extr Metall Rev. 2005. doi: 10.1080/08827500490477603.
12. Associação Brasileira de Normas Técnicas—ABNT. NBR 10004: Resíduos sólidos—Classificação, Rio de Janeiro 2004.
13. Tauber E, Hill RK, Crook DN, Murray MJ. Red mud residues from alumina production as raw material for heavy clay products. J Aust Ceram Soc. 1971;7:12–7.
14. Knight JC, Wagh AS, Reid WA. The mechanical properties of ceramics from bauxite waste. J Mater Sci. 1986. doi:10.1007/BF00547967.
15. Moya JS, Morales F, Garcia AV. Utilizacion cerámica de los barros rojos de las plantas de alumina. Bol Soc Esp Cerám Vidr. 1987;26:21–9.
16. Morales F, Moya JS, De Aza SP. Obtención de ladrillos densos a partir de Barros Rojos, subproducto de las plantas de alúmina. In: Actas II del VIII Congreso-Exposición Argentino y II Iberoamericano de Cerámica, Vidrio y Refractarios, Buenos Aires; 1988. p. 117.
17. Pinnock WR, Gordon JN. Assessment of strength development in Bayer-process residues. J Mater Sci. 1992. doi:10.1007/BF02403881.
18. De La Gandara JLO, Alvarez P. La magnetita en la fabricación de ladrillos para la acumulación de calor. Rev Metal. 1994;30: 135–44.
19. Gordon JN, Pinnock WR, Moore MM. A preliminary investigation of strength development in Jamaican red mud composites. Cem Conc Comp. 1996. doi:10.1016/S0958-9465(96)00027-3.
20. Rodriguez GAP, Rivera FG, De Aza SP. Obtención industrial de materiales cerámicos a partir de lodos rojos del proceso Bayer. Bol Soc Esp Cerám Vidr. 1999;38:220–6.
21. Sglavo VM, Campostrini R, Maurina S, Carturan G, Monagheddu M, Budroni G, Cocco G. Bauxite 'red mud' in the ceramic industry. Part 1: thermal behavior. J Eur Ceram Soc. 2000. doi: 10.1016/S0955-2219(99)00088-6.
22. Sglavo VM, Maurina S, Conci A, Salviati A, Carturan G, Cocco G. Bauxite 'red mud' in the ceramic industry. Part 2: production of clay-based ceramics. J Eur Ceram Soc. 2000. doi:10.1016/S0955-2219(99)00156-9.
23. Alp A, Goral MS. The influence of soda additive on the thermal properties of red mud. J Therm Anal Calorim. 2003. doi:10.1023/A:102519792767.
24. Atasoy A. The comparison of the Bayer process waste on the base of chemical and physical properties. J Therm Anal Calorim. 2007. doi: 10.1007/s10973-005-7671-y.
25. Pascual J, Corpas FA, López-Beceiro J, Benítez-Guerrero M, Artiaga R. Thermal characterization of Spanish Red Mud. J Therm Anal Cal. 2009. doi: 10.1007/s10973-008-9230-9.
26. Palmer SJ, Frost RL. Thermal decomposition of Bayer precipitates formed at varying temperatures J Therm Anal Cal. 2010. doi:10.1007/s10973-009-0136-y.
27. Palmer SJ, Frost RL. Characterisation of bauxite and seawater neutralised bauxite residue using XRD and vibrational spectroscopic techniques. J Mater Sci. 2009. doi:10.1007/s10853-008-3123-y.
28. Rodríguez-Carvajal J. Recent advances in magnetic structure determination by neutron powder diffraction. Phys B Condens Matter. 1993. doi:10.1016/0921-4526(93)90108-I.
29. Smith P. The processing of high silica bauxites—review of existing and potential processes. Hydrometallurgy. 2009. doi: 10.1016/j.hydromet.2009.04.015.
30. Snars K, Gilkes RJ. Evaluation of bauxite residues (red muds) of different origins for environmental applications. Appl Clay Sci. 2009. doi:10.1016/j.clay.2009.06.014.
31. Mackenzie RC. The differential thermal investigation of clays. London: Mineralogical Society; 1957. v. 1, cap. 12, 329–363.
32. Wefers K, Misra C. Oxides and hydroxides of aluminum. Pensilvania, USA: ALCOA, Laboratories; 1987. p. 20.
33. Ingram-Jones VJ, Slade RCT, Davies TW, Southern JC, Salvador S. Dehydroxylation sequences of gibbsite and boehmite: study of differences between soak and flash calcination and of particle-size effects. J Mater Chem. 1996. doi:10.1039/JM9960600073.
34. Rivas Mercury JM, De Aza AH, Turrillas X, Sheptyakov D, Pena, P. On the decomposition of synthetic Gibbsite studied by neutron thermodiffractometry. J Am Ceram Soc. 2006. doi:10.1111/j.1551-2916.2006.01191.x.
35. Derie R, Ghodsiand M, Calvo-Roche C. DTA study of the dehydration of synthetic goethite α-FeOOH. J Therm Anal Cal. 1976. doi:10.1007/BF01909409.
36. Šubrt J, Balek V, Criado JM, Pérez-Maqueda LA, Večerniková E. Characterisation of α-FeOOH grinding products using simultaneous DTA and TG/DTG coupled with MS. J Therm Anal Cal. 1998. doi:10.1023/A:1010197510542.
37. Laskoul M, Margomenou-Leonidopoulou G, Balek V. Thermal characterization of bauxite samples. J Therm Anal Cal. 2006. doi: 10.1007/s10973-005-7126-5.
38. Alp A, Goral MS. The influence of soda additive on the thermal properties of red mud. J Therm Anal Cal. 2003. doi:10.1023/A:1025197927673.
39. Atasoy A. An investigation on the characterization and thermal analysis of the Aughinish red mud. J Therm Anal Cal. 2005. doi: 10.1007/s10973-005-6419-z.
40. Todor DN. Thermal of mineral analysis. 1st ed. Bucharest: Abacus Press; 1976.
41. Bown WE, Dollimore D, Galvey AK. Reactions in the solid state: chemical kinetics, vol. 22, New York: Elsevier; 1980.
42. Whittington B, Ilievski D. Determination of the gibbsite dehydration reaction pathway at conditions relevant to Bayer refineries. Chem Eng J. 2004. doi:10.1016/S1385-8947(03)00207-9.
43. Gan BK, Madsen IC, Hockridge JG. In situ X-ray diffraction of the transformation of gibbsite to alumina through calcination: effect of particle size and heating rate. J Appl Cryst. 2009. doi: 10.1107/S0021889809021232.
44. Mitov I, Paneva D, Kunev B. Comparative study of the thermal decomposition of iron oxyhydroxides. Thermochim Acta. 2002. doi:10.1016/S0040-6031(01)00808-5.
45. Armstrong JA, Dann SE. Investigation of zeolite scales formed in the Bayer process. Microporous Mesoporous Mater. 2000. doi: 10.1016/S1387-1811(00)00276-6.

46. Borchert W, Keidel J. Reactivity of silicates at low temperatures: I. Heildelberg Beitr Mineral Petrogr. 1947;1:12–6.
47. Mead PJ, Weller MT. Synthesis, structure, and characterization of halate sodalites: $M_8[AlSiO_4]_6(XO_3)_x(OH)_{2-x}$; M = Na, Li, or K; X = Cl, Br, or I. Zeolites. 1995. doi:10.1016/0144-2449(95)00004-P.
48. Felsche J, Luger S. Phases and thermal decomposition characteristics of hydro-sodalites $Na_{6+x},[AlSiO_4]_6,(OH)_x{\cdot}nH_2O$. Thermochim Acta. 1987. doi:10.1016/0040-6031(87)80069-2.
49. Schipper DJ, Lathouwers TJ, Van Doorn CZ. Thermal decomposition of sodalites. J Am Ceram Soc. 1973. doi:10.1111/j.1151-2916.1973.tb12402.x.